

# Northumbria Research Link

Citation: Longo, Giulia, Whalley, Lucy, Holland, Adam, Tiwari, Devendra, Durose, Ken, Hutter, Oliver and Kayastha, Prakriti (2023) High temperature equilibrium of 3D and 2D chalcogenide perovskites. Solar RRL, 7 (9). p. 2201078. ISSN 2367-198X

Published by: Wiley-Blackwell

URL: <https://doi.org/10.1002/solr.202201078> <<https://doi.org/10.1002/solr.202201078>>

This version was downloaded from Northumbria Research Link:  
<https://nrl.northumbria.ac.uk/id/eprint/51410/>

Northumbria University has developed Northumbria Research Link (NRL) to enable users to access the University's research output. Copyright © and moral rights for items on NRL are retained by the individual author(s) and/or other copyright owners. Single copies of full items can be reproduced, displayed or performed, and given to third parties in any format or medium for personal research or study, educational, or not-for-profit purposes without prior permission or charge, provided the authors, title and full bibliographic details are given, as well as a hyperlink and/or URL to the original metadata page. The content must not be changed in any way. Full items must not be sold commercially in any format or medium without formal permission of the copyright holder. The full policy is available online: <http://nrl.northumbria.ac.uk/policies.html>

This document may differ from the final, published version of the research and has been made available online in accordance with publisher policies. To read and/or cite from the published version of the research, please visit the publisher's website (a subscription may be required.)



**Northumbria  
University**  
NEWCASTLE



**UniversityLibrary**

# High-Temperature Equilibrium of 3D and 2D Chalcogenide Perovskites

Prakriti Kayastha, Devendra Tiwari, Adam Holland, Oliver S. Hutter, Ken Durose, Lucy D. Whalley,\* and Giulia Longo\*

Chalcogenide perovskites have been recently proposed as novel absorber materials for photovoltaic applications.  $\text{BaZrS}_3$ , the most investigated compound of this family, shows a high absorption coefficient, a bandgap of around 1.8 eV, and excellent stability. In addition to the 3D perovskite  $\text{BaZrS}_3$ , the Ba–Zr–S compositional space contains various 2D Ruddlesden–Popper phases  $\text{Ba}_{n+1}\text{Zr}_n\text{S}_{3n+1}$  (with  $n = 1, 2, 3$ ) which have recently been reported. Herein, it is shown that at high temperature the Gibbs free energies of 3D and 2D perovskites are very close, suggesting that 2D phases can be easily formed at high temperatures. The product of the BaS and  $\text{ZrS}_2$  solid-state reaction, in different stoichiometric conditions, presents a mixture of  $\text{BaZrS}_3$  and  $\text{Ba}_4\text{Zr}_3\text{S}_{10}$ . To carefully resolve the composition, X-ray diffraction, scanning electron microscopy, and energy-dispersive X-ray spectroscopy analysis are complemented with Raman spectroscopy. For this purpose, the phonon dispersions, and the consequent Raman spectra, are calculated for the 3D and 2D chalcogenide perovskites, as well as for the binary precursors. This thorough characterization demonstrates the thermodynamic limitations and experimental difficulties in forming phase-pure chalcogenide perovskites through solid-state synthesis and the importance of using multiple techniques to soundly resolve the composition of these materials.

## 1. Introduction

Chalcogenide perovskites (CPVK) have recently been proposed as possible non-toxic alternatives to lead-based perovskites for photovoltaic applications thanks to their promising optoelectronic characteristics, including a bandgap that is suited for tandem solar cell applications.<sup>[1–4]</sup> Chalcogenide perovskites follow the formula  $\text{ABX}_3$  with A, B, and X representing an alkaline earth cation (2+), a transition metal cation (4+), and a chalcogenide anion (2–), respectively.<sup>[5–7]</sup> The most studied compound in this family is  $\text{BaZrS}_3$ , but other compositions have been reported.<sup>[8,9]</sup>

Accordingly, chalcogenide perovskites have been under recent scrutiny to evaluate and validate a variety of optoelectronic parameters. Reports suggest the possibility of tunable bandgaps through compositional engineering with high absorption coefficients in the visible range,<sup>[10]</sup> low effective masses,<sup>[11]</sup> and, resultantly, high carrier mobilities.<sup>[12]</sup> Moreover, these materials should present improved thermal and

chemical stability compared with the hybrid halide perovskites, being resistant toward high temperatures and atmospheric conditions.<sup>[13]</sup>

Notwithstanding these promising features, the development of CPVK-based devices is still hindered by the synthetic procedure necessary to prepare these perovskites. In practice, these materials need very high temperatures to be crystallized in the desired phase. For example,  $\text{BaZrS}_3$  is produced by the solid-state reaction of the elemental or binary precursors at 800–1100 °C for several hours or days. This requirement for high temperatures is limiting as it does not easily allow for thin film processing and device integration, and can lead to chalcogen loss via volatile precursors.


Understanding reaction mechanisms can help design fabrication procedures potentially having lower temperatures, and recent research has started to explore which processes may allow for this. For example, it has been proposed that favoring the formation of  $\text{BaS}_3$ , which has a lower melting point than BaS, can trigger the formation of  $\text{BaZrS}_3$  at temperatures as low as 600 °C.<sup>[14]</sup> Similarly, it has been reported that an excess of sulfur in the reaction mixture can significantly reduce the reaction time and temperature.<sup>[15]</sup>

P. Kayastha, D. Tiwari, O. S. Hutter, L. D. Whalley, G. Longo  
Department of Mathematics, Physics and Electrical Engineering  
Northumbria University  
Newcastle upon Tyne NE1 8ST, UK  
E-mail: l.whalley@northumbria.ac.uk; g.longo@northumbria.ac.uk

D. Tiwari  
School of Chemistry  
University of Bristol  
Bristol BS8 1TS, UK

A. Holland  
HORIBA UK Limited  
Northampton NN3 6FL, UK

K. Durose  
Department of Physics  
Stephenson Institute for Renewable Energy  
Liverpool L23 9SD, UK

 The ORCID identification number(s) for the author(s) of this article can be found under <https://doi.org/10.1002/solr.202201078>.

© 2023 The Authors. Solar RRL published by Wiley-VCH GmbH. This is an open access article under the terms of the Creative Commons Attribution License, which permits use, distribution and reproduction in any medium, provided the original work is properly cited.

DOI: 10.1002/solr.202201078

The tuning of the precursors' stoichiometry can provide a path to find milder synthetic conditions for  $\text{BaZrS}_3$  and other chalcogenide perovskites, but it can also lead to the formation of other unwanted perovskite phases. The ideal perovskite structure is formed from a 3D network of corner sharing octahedra. However, there are other closely related perovskite-like phases that can be formed. For example, low-dimensional Ruddlesden–Popper (RP) phases are known for chalcogenide perovskites, similar to the oxide and halide perovskites.  $\text{Ba}_{n+1}\text{Zr}_n\text{S}_{3n+1}$  for  $n = 1, 2, 3$  (with the presence of low- and high-temperature polymorphs for  $\text{Ba}_3\text{Zr}_2\text{S}_7$ ) have been reported in addition to the 3D structure  $\text{BaZrS}_3$  (in which  $n = \infty$ ).<sup>[6,13,16–18]</sup> For the corresponding perovskites with Hf ( $\text{Ba}_{n+1}\text{Hf}_n\text{S}_{3n+1}$ ), additional RP phases with  $n = 4, 5$  have been reported,<sup>[19]</sup> while no evidence is present for  $n > 3$  in the Zr series. In these low-dimensional phases, layers of 3D CPVK are alternated with layers of BaS, as represented in Figure 1. Interestingly, the bandgaps of these chalcogenide RP perovskites decrease as  $n$  increases, contrary to the oxide and halide counterparts, where the bandgap widens as  $n$  increases.<sup>[20–22]</sup> The different crystalline structure not only affects the bandgap of the perovskite, but can also affect other functional features, such as carrier transport and thermal or chemical stability. A deep understanding of the synthetic reaction, especially when nonstoichiometric conditions are explored, will be essential to control the formation of competing phases with distinct properties.

The most widely used technique for the assessment of different phases is X-ray diffraction (XRD). However, due to the structural similarity of the 3D and the 2D perovskites, the diffractogram peaks overlap, which make differentiating between species challenging. For example, in the case of samples formed

by the mixture of  $\text{BaZrS}_3$  and  $\text{Ba}_3\text{Zr}_2\text{S}_7$ , long data collection times and rigorous refinement (supported by compositional techniques such as energy-dispersive X-ray spectroscopy, EDS) are necessary to give a quantitative estimation of their compositions. As such, even with diffractograms presenting good angular resolution, intensity, and angular range, ambiguous assignment can still occur. It follows that good practice, especially for this family of materials, would be to combine crystallographic analysis with other complementary techniques that may also provide a clearer distinction between species. Vibrational spectroscopy is a good candidate technique to carry out this role, as it probes the local structure of a material, in contrast to XRD which probes the bulk response. In this article, it will be shown that the 3D and 2D perovskite structures each have a unique vibrational fingerprint that better distinguishes between materials in the Ba–Zr–S system and that Raman spectroscopy is therefore well suited for checking the phase purity of the compounds.

In this study, XRD and Raman spectroscopy are combined to assess the main composition of the product resulting from the solid-state reaction of BaS and  $\text{ZrS}_2$  at various ratios. To aid in our analysis, a first-principles thermodynamic model is used to demonstrate that at high temperatures the Gibbs free energy of the 3D and 2D CPVK materials is only a few  $\text{kJ mol}^{-1}$  apart, indicating that both can be formed during high-temperature synthesis ( $>1000$  K). In addition, the Raman spectra for all known binary and ternary compositions in the Ba–Zr–S phase systems are calculated from first principles. Despite the use of excess  $\text{ZrS}_2$  in the reaction mixtures, all the resulting powders show deficiency of Zr and S, and present mixtures of  $\text{BaZrS}_3$  and the RP phase  $\text{Ba}_4\text{Zr}_3\text{S}_{10}$ . It will also be shown that peaks' assignment can be done more confidently when Raman and XRD are

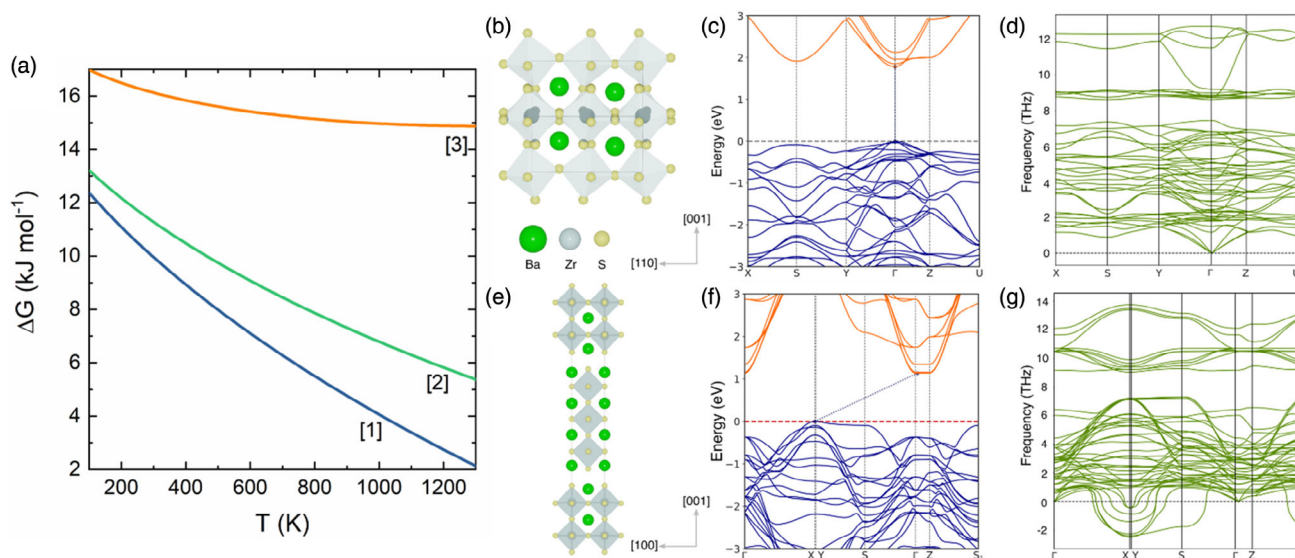


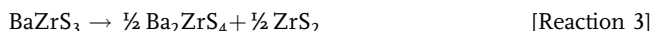
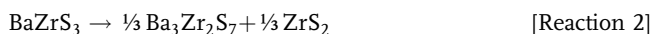
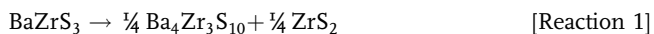
**Figure 1.** Thermodynamic, electronic, and vibrational properties of  $\text{BaZrS}_3$  ( $Pnma$ ) and  $\text{Ba}_{n+1}\text{Zr}_n\text{S}_{3n+1}$  ( $I4/mmm$ ). a) Gibbs free energy  $\Delta G$  as a function of temperature.  $\Delta G$  is calculated for decomposition of  $\text{BaZrS}_3$  into: 1)  $\text{Ba}_4\text{Zr}_3\text{S}_{10}$  and  $\text{ZrS}_2$ ; 2)  $\text{Ba}_3\text{Zr}_2\text{S}_7$  and  $\text{ZrS}_2$ ; 3)  $\text{Ba}_2\text{ZrS}_4$  and  $\text{ZrS}_2$ . For comparison, all materials are in the  $I4/mmm$  phase. b) Crystal structure of  $\text{BaZrS}_3$ . c) Electronic band structure of  $\text{BaZrS}_3$  calculated using the HSE06 exchange–correlation functional and with spin–orbit coupling (SOC), showing a direct bandgap of 1.72 eV. d) Phonon band structure of  $\text{BaZrS}_3$  with positive phonon modes across the Brillouin Zone, indicating dynamical stability. e) Crystal structure of  $\text{Ba}_4\text{Zr}_3\text{S}_{10}$ . f) Electronic band structure of  $\text{Ba}_4\text{Zr}_3\text{S}_{10}$  (HSE06 + SOC), showing an indirect bandgap of 1.13 eV. g) Phonon band structure of  $\text{Ba}_4\text{Zr}_3\text{S}_{10}$  showing negative phonon modes at the zone boundaries, and indicating the presence of a lower symmetry structure at 0 K.

used simultaneously. All calculated Raman spectra and the thermodynamic analysis code are published in open-access repositories alongside this work, allowing the adoption of our approach to other studies of BaZrS<sub>3</sub> synthesis.

## 2. Results and Discussion

During BaZrS<sub>3</sub> synthesis, competing phases can form from both the constituent elements (Ba, Zr, S) and/or from external impurities (e.g., O<sub>2</sub>). In order to focus our analysis efforts on the thermodynamically accessible competing phases, ab initio thermodynamic calculations were performed. As in this study synthesis was carried out within a closed ampule under vacuum, phases in the Ba–Zr–S system only were considered. Competing phases were initially identified using the Materials Project database,<sup>[23]</sup> followed by recalculation of the total energies using a higher level of theory (HSE06 functional with spin–orbit coupling) to reproduce lattice constants and bandgaps in agreement with published results from experimental studies: the formation energy, lattice constants, electronic bandgap, and a comparison to experimental data for all systems considered are provided in Table S1, Supporting Information. Five competing ternary phases were identified: Ba<sub>4</sub>Zr<sub>3</sub>S<sub>10</sub> (*I4/mmm*), Ba<sub>3</sub>Zr<sub>2</sub>S<sub>7</sub> (*I4/mmm*), Ba<sub>3</sub>Zr<sub>2</sub>S<sub>7</sub> (*P4<sub>2</sub>/mnm*), Ba<sub>3</sub>Zr<sub>2</sub>S<sub>7</sub> (*Cmmm*) and Ba<sub>2</sub>ZrS<sub>4</sub> (*I4/mmm*). All ternary compounds are in the RP perovskite analogue series, Ba<sub>n+1</sub>Zr<sub>n</sub>S<sub>3n+1</sub>.

It follows that there are three ternary-to-ternary decomposition mechanisms to consider



To predict the relative phase stabilities, a previously published methodology was followed to calculate the change in Gibbs free energy ( $\Delta G$ ) of each process,<sup>[24,25]</sup> as this is the potential that is minimized in equilibrium. It is important to emphasize that this calculation does not consider the effects of lattice expansion or anharmonic vibrations. However, despite these limitations, this methodology has been used to successfully predict the temperature–pressure stability window for Cu<sub>2</sub>ZnSnS<sub>4</sub>.<sup>[24]</sup>

The  $\Delta G$  for all processes, reported in Figure 1a, is endothermic (positive valued) across the full temperature range considered (100–1300 K).  $\Delta G$  for [Reaction 3] ranges from 17 to 15 kJ mol<sup>−1</sup>, suggesting that BaZrS<sub>3</sub> is stable against decomposition into Ba<sub>2</sub>ZrS<sub>4</sub>.  $\Delta G$  for [Reaction 2] is calculated for the three polymorphs of Ba<sub>3</sub>Zr<sub>2</sub>S<sub>7</sub>. At 300 K  $\Delta G$  is comparable for all three polymorphs, as expected given the structural similarity: 10 kJ mol<sup>−1</sup> (*P4<sub>2</sub>/mnm* and *Cmmm*), 11 kJ mol<sup>−1</sup> (*I4/mmm*). At 1300 K  $\Delta G$  is reduced to very small values: 7 kJ mol<sup>−1</sup> (*P4<sub>2</sub>/mnm*), 6 kJ mol<sup>−1</sup> (*I4/mmm*), and 5 kJ mol<sup>−1</sup> (*Cmmm*).  $\Delta G$  for [Reaction 1] is 10 kJ mol<sup>−1</sup> at RT reducing to 2 kJ mol<sup>−1</sup> at 1300 K. Given that chemical accuracy is  $\approx 4$  kJ mol<sup>−1</sup>, these results indicate that 1) metastable Ba<sub>3</sub>Zr<sub>2</sub>S<sub>7</sub> and Ba<sub>4</sub>Zr<sub>3</sub>S<sub>10</sub> are energetically accessible during synthesis, with Ba<sub>4</sub>Zr<sub>3</sub>S<sub>10</sub> being the most likely phase to form; and 2) formation of Ba<sub>3</sub>Zr<sub>2</sub>S<sub>7</sub> and Ba<sub>4</sub>Zr<sub>3</sub>S<sub>10</sub> becomes more likely as the

temperature is increased. Our results are supported by reports of Ba<sub>4</sub>Zr<sub>3</sub>S<sub>10</sub> formation during high-temperature synthesis of Ba<sub>3</sub>Zr<sub>2</sub>S<sub>7</sub>.<sup>[6]</sup>

Crystal, electronic, and vibrational structure information for BaZrS<sub>3</sub> and for the lowest energy competing phase, Ba<sub>4</sub>Zr<sub>3</sub>S<sub>10</sub> are shown in Figure 1b–g. The electronic band structure is calculated with the HSE06 functional and includes spin–orbit effects, leading to an accurate predicted value of 1.72 eV for the 3D perovskite direct bandgap<sup>[26]</sup> and a predicted value of 1.13 eV for the indirect bandgap of the RP phase. This is the smallest predicted bandgap for RP Ba<sub>n+1</sub>Zr<sub>n</sub>S<sub>3n+1</sub> materials considered, and is in line with previous reports of a decreasing bandgap with increasing *n*.<sup>[20–22]</sup> While an indirect bandgap can lead to a decreased absorption coefficient near the band edge, we expect this to be counter-balanced by the flatter band dispersion for Ba<sub>4</sub>Zr<sub>3</sub>S<sub>10</sub>, resulting in a larger density of states.

At room temperature, BaZrS<sub>3</sub> is reported to form in in space group *Pnma*,<sup>[9]</sup> which is a distortion of the idealized cubic perovskite. RP phases are reported to form in the space group *I4/mmm*.<sup>[20,21]</sup> It is found that BaZrS<sub>3</sub> in the *Pnma* phase is dynamically stable with positive phonon modes across the Brillouin zone. In contrast, Ba<sub>4</sub>Zr<sub>3</sub>S<sub>10</sub> is dynamically unstable with imaginary phonon modes at the zone boundaries. This indicates the presence of a symmetry lowering transition to a more stable phase at low temperature, which is a common feature of halide and oxide perovskite materials.<sup>[27,28]</sup> Ba<sub>4</sub>Zr<sub>3</sub>S<sub>10</sub> in the space group *Fmmm* has also been previously reported in the literature.<sup>[18]</sup> However, this corresponds to a small lattice expansion and increase in the *c/a* lattice parameter ratio, so is unlikely to result from distortions along zone boundary phonon modes of the *I4/mmm* phase. In Figure S1, Supporting Information, we confirm that the high-temperature structures for Ba<sub>4</sub>Zr<sub>3</sub>S<sub>10</sub> (*Fmmm*), Ba<sub>3</sub>Zr<sub>2</sub>S<sub>7</sub> (*I4/mmm*), and Ba<sub>2</sub>ZrS<sub>4</sub> (*I4/mmm*) also produce imaginary phonon modes in the harmonic approximation.

To characterize the bulk structure, XRD was performed on powder samples at room temperature and ambient atmosphere. The corresponding diffractograms are reported in Figure 2a. The names Zr\_0, Zr\_5, Zr\_10, and Zr\_20 used in this work represent the product obtained by the reaction of 1:1, 1:1.05, 1:1.1, 1:1.2 BaS:ZrS<sub>2</sub> molar ratios, respectively.

Observing the diffractograms it can be noted that the samples present high crystallinity and, except the Zr\_20, present complete conversion to the ternary phase, with no evidence of unreacted BaS (Figure S3a, Supporting Information). The presence of unreacted ZrS<sub>2</sub> is more challenging to assess, as its characteristics peak is located at 32.2° (Figure S3a, Supporting Information), where the samples present numerous small peaks which could derive also from the 2D or 3D perovskite. As discussed later in the text, Raman analysis simplified the assignment, confirming the presence of ZrS<sub>2</sub> in the Zr\_0 sample. The Zr\_20 sample presents an additional peak at low angles which origin has not been identified. Given the poor quality of the XRD pattern of this sample, both in terms of crystallinity and phase purity, it has been excluded from further characterization. It has to be noted that the presence of other Ba–S and Zr–S binary compositions has been excluded observing their XRD patterns and Raman spectra (Figure S3b, Supporting Information). Similarly, the presence of oxides, sulfates, and carbonates (all possible unwanted products in presence of air) has been



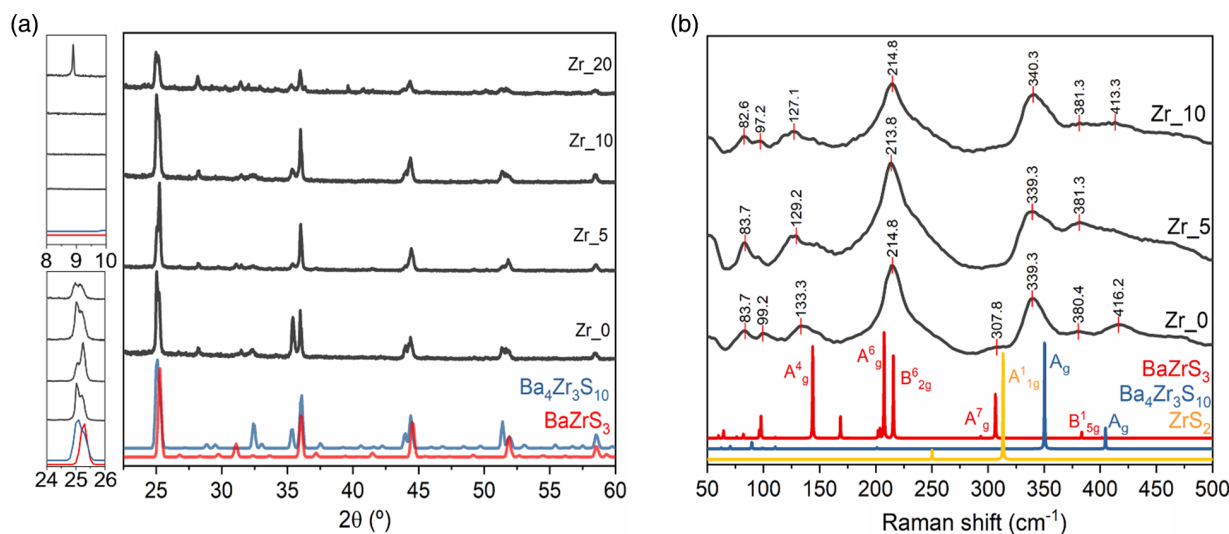


**Figure 2.** a) X-ray diffractograms of the synthesized powders. Reference patterns for  $\text{BaZrS}_3$ ,  $\text{Ba}_4\text{Zr}_3\text{S}_{10}$  are taken from ICSD (Collection Code 23288 and 72656, respectively). Top left panel: focus on the low-angle peak shown by  $\text{Zr}_{20}$ . Bottom left panel: focus of the main peak. b) Calculated (bottom) and measured (top) Raman spectra collected with 785 nm excitation wavelength.

excluded by comparing reported experimental XRD patterns and Raman spectra (Table S3, Supporting Information).

The  $\text{Zr}_0$  sample, which was expected to provide stoichiometric conversion to  $\text{BaZrS}_3$ ,<sup>[29]</sup> shows the presence of multiple phases that were assigned to the 3D  $\text{BaZrS}_3$  and to the RP phase  $\text{Ba}_4\text{Zr}_3\text{S}_{10}$ . It is important to highlight the similarity of the angular position and intensity of the  $\text{BaZrS}_3$ ,  $\text{Ba}_3\text{Zr}_2\text{S}_7$ , and  $\text{Ba}_4\text{Zr}_3\text{S}_{10}$  XRD patterns, which complicates the experimental diffractograms resolution (Figure S4, Supporting Information). The Rietveld refinement presented in Figure S5 and Table S4–S6, Supporting Information, shows that the RP phase is the majority one, representing almost the 70% by mass. As the molar amount of  $\text{ZrS}_2$  in the starting mixture is increased by 5%, the diffractogram still reveals a mixture of phases, but with an overall predominance of the  $\text{BaZrS}_3$  over the RP phase.

This can be concluded by the change in shape of the peak at  $25.1^\circ$  and by observing the high-angle peaks (Figure S4, Supporting Information), and is confirmed by the Rietveld refinement. For the sample with a nominal 10% molar excess of  $\text{ZrS}_2$ ,  $\text{Ba}_4\text{Zr}_3\text{S}_{10}$  returns to be the majority phase, surprisingly reaching 86% of the sample weight (Table 1).

In Figure 2b and Table 2, the experimentally recorded Raman spectra of all the samples are reported together with the calculated spectra of  $\text{BaZrS}_3$ ,  $\text{Ba}_4\text{Zr}_3\text{S}_{10}$ , and  $\text{ZrS}_2$ . First of all, it is worth stressing that the Raman spectra allow clear distinction between the binary sulfides, the 2D RP phases, and 3D

**Table 1.** Phase quantification from Rietveld refinement.

	$\text{BaZrS}_3$ ( <i>Pnma</i> ) [wt%]	$\text{Ba}_4\text{Zr}_3\text{S}_{10}$ ( <i>Fmmm</i> ) [wt%]	$\text{BaZrS}_3$ ( <i>Pnma</i> ) [mol%]	$\text{Ba}_4\text{Zr}_3\text{S}_{10}$ ( <i>Fmmm</i> ) [mol%]
$\text{Zr}_0$	31	69	61	39
$\text{Zr}_5$	59	41	84	16
$\text{Zr}_{10}$	14	86	36	64

**Table 2.** Raman peak positions for the measured  $\text{Zr}_0$  ( $\nu_{\text{exp}}$ ) compared to the calculated value ( $\nu_{\text{pbisol}}$ ).

Material	Mode	$\nu_{\text{pbisol}}$	$\nu_{\text{exp}}$
$\text{BaZrS}_3$	$\text{A}_g^3$	94.0	83.7
	$\text{A}_g^4$	139.8	133.3
	$\text{A}_g^6$	204.9	214.8
	$\text{B}_g^{6_{2g}}$	213.1	214.8
	$\text{B}_g^{5_{1g}}$	389.1	380.4
$\text{ZrS}_2$	$\text{A}_g^{1_{1g}}$	313.4	307.8
$\text{Ba}_4\text{Zr}_3\text{S}_{10}$	$\text{A}_g$	350.1	339.3
	$\text{A}_g$	403.9	416.2

CPVK, in contrast with the XRD pattern in Figure 2a. At a first look it can already be appreciated that in all the samples there is  $\text{BaZrS}_3$ , as shown by the most intense peak located at  $214\text{ cm}^{-1}$ , deriving from the  $\text{A}_g^6$  and  $\text{B}_g^{6_{2g}}$  vibrational modes. Similarly, the peaks at lower frequencies (83 and  $133\text{ cm}^{-1}$ ) and the peak at  $380\text{ cm}^{-1}$  are mainly assigned to the  $\text{BaZrS}_3$  phase ( $\text{A}_g^3$ ,  $\text{A}_g^4$ , and  $\text{B}_g^{5_{1g}}$ , respectively), in agreement with previous works (Table 2).<sup>[5,28–30]</sup> It is worth stressing that the expected experimental spectra measured at room temperature should be redshifted to lower frequencies compared to computational predictions, due to thermal expansion of the lattice which leads to a softening of the phonon modes. For the  $\text{A}_g^3$  and  $\text{A}_g^4$  modes in  $\text{BaZrS}_3$ , the frequency shift at room temperature is reported to be approximately  $8\text{ cm}^{-1}$ ,<sup>[31]</sup> in agreement with what observed (a shift of  $10.3$  and  $6.6\text{ cm}^{-1}$ , respectively). In contrast, the experimental spectra are blueshifted for the  $\text{A}_g^6$  and  $\text{B}_g^{6_{2g}}$  modes, as has been reported previously.<sup>[31,32]</sup> Importantly, these modes relate to displacements of the sulfur species only. In the sample  $\text{Zr}_0$ , a shoulder can be observed around  $308\text{ cm}^{-1}$ , which is assigned to both the  $\text{A}_g^7$  mode of the  $\text{BaZrS}_3$  and the  $\text{A}_g^{1_{1g}}$  of the  $\text{ZrS}_2$ .

As previously reported Raman spectra of BaZrS<sub>3</sub> show that the A<sub>g</sub><sup>7</sup> mode is visible only at low temperature,<sup>[31]</sup> the 308 cm<sup>-1</sup> peak in the Zr<sub>0</sub> spectrum is likely to derive from unreacted ZrS<sub>2</sub>. This demonstrates that the presence of ZrS<sub>2</sub> is easier to observe through Raman spectroscopy than through XRD.

Importantly, all the spectra present a peak at around 339 cm<sup>-1</sup> which does not derive from the 3D perovskite. Comparing the measured spectrum with the calculated one for Ba<sub>4</sub>Zr<sub>3</sub>S<sub>10</sub> it is possible to assign it to the secondary RP phase, which is also corroborated by XRD. The Zr<sub>0</sub> sample presents an additional peak at 416 cm<sup>-1</sup>, which can be assigned to the A<sub>g</sub> mode of the Ba<sub>4</sub>Zr<sub>3</sub>S<sub>10</sub>. This phonon mode involves displacement of the sulfur species only, as in the A<sub>g</sub><sup>6</sup> and B<sub>2g</sub><sup>6</sup> modes of the BaZrS<sub>3</sub> phase, which can be used to rationalize the unexpected blue shift to higher frequencies for the experimental spectra.

Importantly, Raman spectra cannot be used for quantitative analysis unless calibration with phase pure materials is performed. The higher intensity of the BaZrS<sub>3</sub> Raman peaks compared to the RP ones does not indicate a higher content in the sample, as demonstrated by the Rietveld quantifications. However, it is interesting to note how the ratio between the areas of the 339 and 214 cm<sup>-1</sup> peak decreases as 5% molar excess of ZrS<sub>2</sub> is used in the starting mixture, suggesting that in this sample the orthorhombic 3D phase is favored over the 2D. This hypothesis is supported by the disappearance of the peak at 99 cm<sup>-1</sup> (which does not derive from BaZrS<sub>3</sub> and is attributed to the Ba<sub>4</sub>Zr<sub>3</sub>S<sub>10</sub> mode located at 92 cm<sup>-1</sup>) and to the increased intensity of the 380 cm<sup>-1</sup> peak. In the Zr<sub>10</sub> sample, instead, the ratio between the two peaks returns in favor to the Ba<sub>4</sub>Zr<sub>3</sub>S<sub>10</sub>, with a reduction of the BaZrS<sub>3</sub> peaks, as confirmed by Rietveld analysis. It should be noted that the measured Raman spectra were compared against the spectra of the binary precursors (Figure S3, Supporting Information) as well as against the oxide counterparts (Table S3, Supporting Information),<sup>[33–37]</sup> confirming their absence in the synthesized mixture.

So far it has been shown that, in these synthetic conditions, the reaction between binary precursors leads to the formation of a secondary 2D ternary phase. Zr- or S-poor conditions can trigger the formation of RP phases, and a careful compositional analysis is necessary to obtain sensible conclusions. For this reason, EDS compositional analysis has been performed on all the synthesized powders and on the Zr<sub>0</sub> precursor mixture before heat treatment, and the results are reported in Table 3.

The Zr<sub>0</sub> precursor mixture confirms that the Ba/Zr atomic ratio before heat treatment was 1:1. Surprisingly, all the resulting powders after treatment present Zr deficient compositions, with the Ba/Zr atomic ratio decreasing in the Zr<sub>0</sub>, Zr<sub>5</sub> and Zr<sub>10</sub>

series. However it is worth stressing that the confidence range of these values is enlarged by the limitations associated with powders analysis with EDS (see Supporting Information). The starting material and the synthesized powders also present substoichiometric amounts of sulfur, which become more unbalanced as the starting excess of ZrS<sub>2</sub> is higher. To exclude accidental losses during the loading of the samples in the quartz ampules, a second batch repeating the Zr<sub>0</sub> conditions was prepared and characterized showing very similar XRD, Raman spectra, and EDS compositions to Zr<sub>0</sub> (Figure S6, Supporting Information). The systematic loss of Zr in these synthesis hints to possible unwanted reactions with the quartz ampule, even if carbon-coated. More investigation is needed to address this phenomenon, which is out of the scope of this work. However, this evidence hints that other precursors, rather than ZrS<sub>2</sub>, should be used, especially in high-temperature solid-state synthesis.

The observation of substoichiometric amounts of Zr and S gives an additional explanation for the formation of Ba<sub>4</sub>Zr<sub>3</sub>S<sub>10</sub>. As the RP Ba<sub>n+1</sub>Zr<sub>n</sub>S<sub>3n+1</sub> family of materials are a ZrS<sub>2</sub>-deficient analogue of BaZrS<sub>3</sub>, the RP phases are expected to be more readily formed in Zr- or S-poor environments. To explore this further, a ternary phase diagram for the Ba–Zr–S system was constructed using the first-principles thermodynamic model introduced earlier (Figure S2, Supporting Information). This allows a prediction of which products are formed for the substoichiometric amounts of Zr and S as measured by EDS. At high temperature, all RP phases and most binary phases (all except BaS<sub>3</sub>) lie on the convex hull, so that the predicted products are very sensitive to composition. Using Ba–Zr–S composition values within the range of values reported for each sample in Table 3, the model predicts that Ba<sub>4</sub>Zr<sub>3</sub>S<sub>10</sub> and BaZrS<sub>3</sub> will be formed at 900 °C, alongside a smaller proportion of ZrS<sub>2</sub> (Table S7, Supporting Information). This suggests that there is an additional driving force for phase separation into BaZrS<sub>3</sub> and Ba<sub>4</sub>Zr<sub>3</sub>S<sub>10</sub> resulting from the under stoichiometric amount of Zr and S. Our modeling also suggests that the S concentration in the samples limits the formation of BaZrS<sub>3</sub>. This is why the Zr<sub>10</sub> sample, with the lowest proportion of sulfur measured by EDS, produces the highest proportion of Ba<sub>4</sub>Zr<sub>3</sub>S<sub>10</sub>. On the other hand, this sample has the Ba/Zr ratio closer to unity, suggesting that the cation ratio is not the driving force for the preferential formation of 3D over 2D perovskites.

The compositional mapping presented in Figure 3 offers an additional insight in the nature of the synthesized powders. In the image, brighter zones correspond to areas of high atomic concentration, although it is recognized that shadowing effects give large dark areas (observable in the dark large areas in the mappings but not in the secondary electron images). Notwithstanding this, it may be observed that in all the samples Zr is less uniformly distributed than Ba and S, as evidenced by the particularly bright area in the Zr mapping. Among all the samples, the Zr<sub>0</sub> shows the biggest agglomeration of zirconium. Brighter area can be observed also in the other samples, but the dimension and number of these agglomerates reduces in Zr<sub>5</sub> and Zr<sub>10</sub> with the formation of smaller clusters more dispersed across the sample. The EDS analysis confirmed the presence of Zr-rich clusters in the sample Zr<sub>0</sub> (Figure S7, Supporting Information), but in the others the distribution of Zr looks more homogeneous (Figure S8 and S9, Supporting

**Table 3.** EDS quantifications (in atomic %) of the Zr<sub>0</sub> powder before the synthesis and after, Zr<sub>5</sub> and Zr<sub>10</sub> with the instrumental error.

	Ba	Zr	S
Zr <sub>0</sub> before treatment	23 ± 5	22 ± 5	55 ± 5
Zr <sub>0</sub> after treatment	25 ± 5	21 ± 5	54 ± 5
Zr <sub>5</sub>	25 ± 5	22 ± 5	53 ± 5
Zr <sub>10</sub>	25 ± 5	23 ± 5	52 ± 5



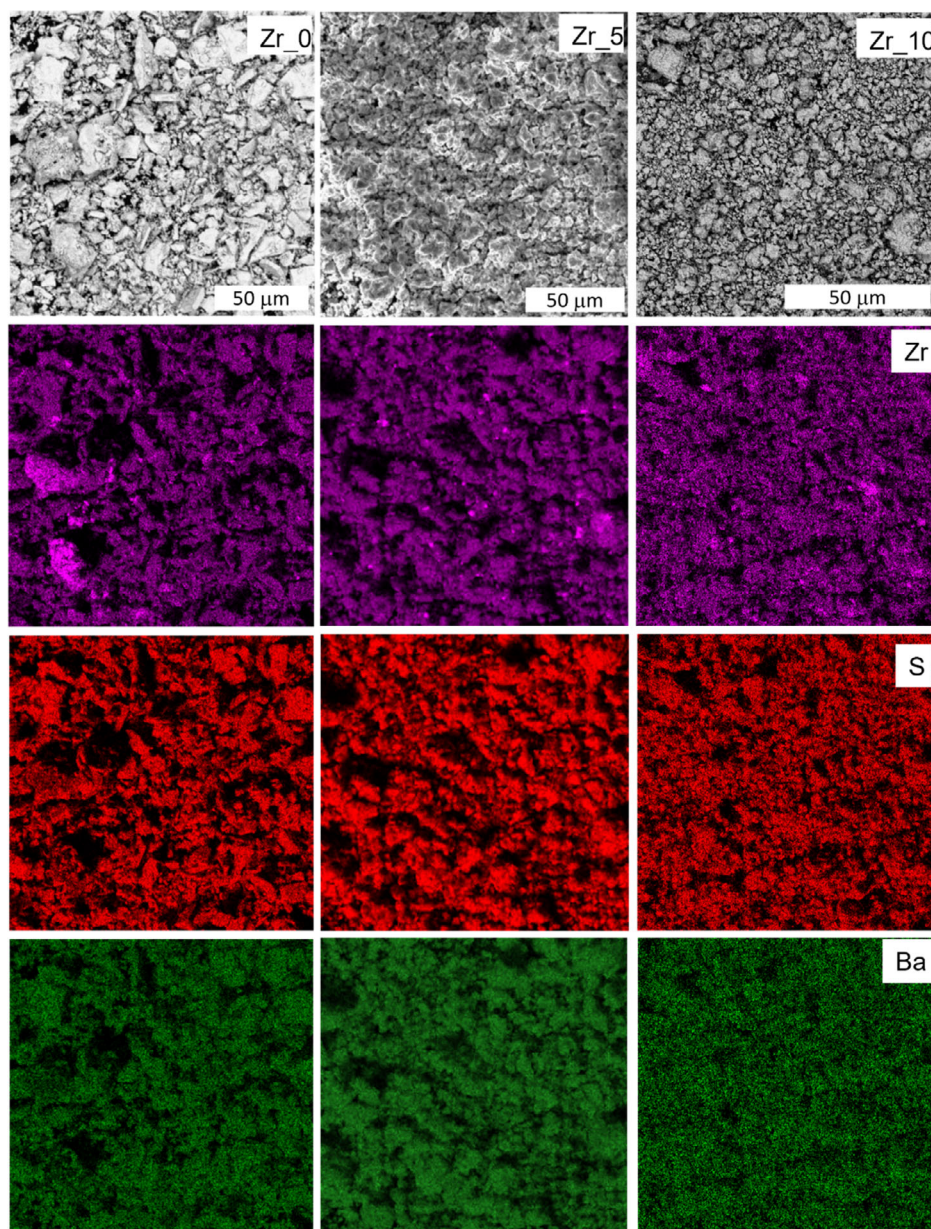


**Figure 3.** Secondary electron images and elemental mapping of the Zr\_0, Zr\_5, and Zr\_10 (left, center, and right column, respectively).

Information), even if some local deviations from the average are still present, as indicated by the mapping results. Instead, Ba and S mapping shows that the Zr-rich areas in the Zr\_0 sample correspond to S and Ba deficient zones. The presence of Zr-rich clusters hinders the uniformity of the reaction environment possibly creating local regions even more Zr-deficient than the average composition, favoring the formation of 2D perovskites. Furthermore, the morphology of the synthesized crystals has been analyzed through scanning electron microscopy (SEM) in both secondary electron and the more compositionally sensitive backscattered electron (BSE) modes. Looking at the BSE image in Figure S10, Supporting Information, it can be noted that, in the Zr\_0 sample, the crystals have a different appearance accordingly with the grain composition, as it could also be

appreciated in Figure S7, Supporting Information. The grains with a composition close to stoichiometry have a flat, uniform surface, while the grains presenting high concentrations of Zr present an irregular, rough, patchy microstructure within the grain. Additionally, it can be observed that the flat and regular grains present a laminar structure, further indication of the presence of layered 2D phases in the sample.

### 3. Conclusions

In this work, experimental and computational techniques have been combined to identify structurally similar products of the reaction between BaS and ZrS<sub>2</sub> at different stoichiometric ratios.

Ab initio thermodynamic calculations identified that chalcogenide RP phases (and in particular the phases with larger  $n$ ) are energetically close to  $\text{BaZrS}_3$  and are thermodynamically accessible at the high temperatures often required for the CPVK synthesis. XRD and Raman spectroscopy demonstrate that for all the investigated ratios of binary chalcogenide precursors, mixtures of 3D  $\text{BaZrS}_3$  and 2D  $\text{Ba}_4\text{Zr}_3\text{S}_{10}$  are created. Interestingly, it has been shown that, despite the use of  $\text{ZrS}_2$  excess in the precursor mixtures, Zr and S deficiencies have been observed in all the synthesized powders, further driving the 2D phase formation. However, the formation of RP phase does not depend only on the Ba/Zr ratio (with higher concentration of 2D phases formed with the Ba/Zr ratio closer to unity), but is also extremely sensitive to sulfur deficiencies. These results suggest the high possibility of creation of mixed phases during CPVK synthesis at high temperatures, and the need to carefully control phase composition. These results may also explain why the reported bandgap of  $\text{BaZrS}_3$  varies significantly in different publications: it is possible that 3D and 2D mixtures were created and not identified due to the similarity of the XRD diffractograms of these species.

Raman spectra calculated from first principles have been published in an open-source database for binary Ba–S and Zr–S and ternary Ba–Zr–S compositions. This includes Raman data not yet present in the literature, specifically for phases  $\text{Ba}_4\text{Zr}_3\text{S}_{10}$ ,  $\text{BaS}_2$ ,  $\text{BaS}_3$ ,  $\text{ZrS}$ , and  $\text{ZrS}_3$ .  $\text{Ba}_4\text{Zr}_3\text{S}_{10}$  has been rarely reported, and little characterization is available in literature on this RP perovskite. The DFT calculations presented predict an indirect bandgap of 1.13 eV, suggesting that it is the smallest bandgap of materials synthesized in the  $\text{Ba}_{n+1}\text{Zr}_n\text{S}_{3n+1}$  series.

Finally, this work has demonstrated the complexity of the Ba–Zr–S phase diagram, stressing the importance of using multiexperimental techniques to soundly resolve the reaction products of synthesis, and the necessity to find alternative synthetic routes involving lower temperatures and different precursors. Raman spectroscopy, here suggested as a technique complementary to XRD, has been proven to provide a relatively easy and quick differentiator between CPVK phases, and even for several binary compositions of the Ba–Zr–S elements. In addition, the use of Raman spectroscopy in other CPVK synthesis environments (such as nanoparticle synthesis) may help to identify the reaction mechanisms where traditional techniques, such as XRD, cannot be used, or where the presence of organic materials complicates the analysis. Hopefully, the use of the database created in this work will support further progress in developing a low-temperature synthetic procedure for chalcogenide perovskites, promote increased control of the 2D–3D phase equilibrium during synthesis, and ultimately enable their thin film deposition and integration into optoelectronic devices.

## 4. Experimental Section

**Experimental Procedure:** Synthesis of powders: BaS (99.7%, Alfa Aesar) and  $\text{ZrS}_2$  (99.99%, Alfa Chemistry) were used without further purification. 300 mg of powder formed by 1:1, 1:1.05, 1:1.1, and 1:1.2 molar mixtures of BaS and  $\text{ZrS}_2$  (called Zr\_0, Zr\_5, Zr\_10, Zr\_20, respectively) were finely ground with an agate pestle and mortar, loaded into carbon-coated quartz ampules, purged with argon 3 times and sealed under a vacuum of  $10^{-5}$  mbar. Each mixture was then placed in a single zone furnace at 500 °C, and the temperature was increased to 900 °C at a rate of

200 °C h<sup>-1</sup>. The powders were kept at 900 °C for 5 days, and finally quenched in water.

**Computational Details:** Competing phases of  $\text{BaZrS}_3$  were identified using the Materials Project database,<sup>[38]</sup> with all Ba–Zr–S compounds within 0.5 eV above the convex hull considered. This energy range has been shown to cover the 90th percentile of all metastable materials reported within Materials Project.<sup>[39,40]</sup> First-principles density functional theory (DFT) calculations were carried out with the all-electron numeric atom-centered code FHI-aims.<sup>[41]</sup> Minimum-energy crystal structures were found using parametrically constrained geometry relaxation.<sup>[42]</sup> The self-consistent field criterion was set to  $10^{-7}$  e Å<sup>-3</sup> and  $10^{-6}$  eV Å<sup>-1</sup> for electron density and force, respectively. The structures were relaxed until the maximum force component was below  $5 \times 10^{-3}$  eV Å<sup>-1</sup>. All other inputs were set to the default value within FHI-aims. All relaxations and phonon calculations were performed with the PBEsol<sup>[43]</sup> functional with a tight basis set. Electronic band structures and total energies were calculated using the HSE06<sup>[44]</sup> functional alongside inclusion of spin–orbit coupling. The resulting formation energies and bandgaps are reported in Table S1, Supporting Information. Phonon band structures were evaluated using the finite difference method with a 0.01 Å step size, as implemented in Phonopy.<sup>[45]</sup> The supercell size and  $k$ -point spacing used for phonon calculations are presented in Table S2, Supporting Information. Raman intensities and peak positions were generated through Phonopy-Spectroscopy with a two-point finite difference along displacements, and are reported in the Supporting Information.<sup>[46]</sup> A Lorentzian peak width of 1 cm<sup>-1</sup> was set on the peak positions obtained from the analysis. Macroscopic dielectric tensors were evaluated using the real space density functional perturbation theory method implemented in FHI-aims<sup>[47]</sup> with the PBE functional.<sup>[48]</sup> Gibbs free energies were calculated using Phonopy and the ThermoPot package.<sup>[49]</sup> Imaginary modes were omitted from our calculation of the thermodynamic partition function and so do not contribute to the Gibbs free energy. An online repository containing 1) analysis code for generating Figure 1a and S2, Supporting Information; 2) the raw data from electronic structure calculations; and 3) the data used to generate Raman spectra is available at [https://github.com/NU-CEM/2022\\_BaZrS3\\_High-T\\_equilibrium](https://github.com/NU-CEM/2022_BaZrS3_High-T_equilibrium).

## Supporting Information

Supporting Information is available from the Wiley Online Library or from the author.

## Acknowledgements

P.K. and L.D.W. thank Jonathan M. Skelton for discussions on Phonopy-Spectroscopy. P.K. and G.L. acknowledge support from the UK Engineering and Physical Sciences Research Council (EPSRC) CDT in Renewable Energy Northeast Universities (ReNU) for funding through EPSRC Grant EP/S023836/1. The authors thank Horiba for the support with the Raman measurements. This work used the Oswald High Performance Computing facility operated by Northumbria University (UK). Via our membership of the UK's HEC Materials Chemistry Consortium, which is funded by EPSRC (EP/R029431), this work used the ARCHER2 UK National Supercomputing Service.

## Conflict of Interest

The authors declare no conflict of interest.

## Data Availability Statement

The data that support the findings of this study are openly available in Zenodo at <https://zenodo.org/record/7391360>, reference number 7391360.



## Keywords

Ba<sub>4</sub>Zr<sub>3</sub>S<sub>10</sub>, BaZrS<sub>3</sub>, chalcogenide perovskites, high-temperature syntheses, Raman spectroscopy, Ruddlesden–Popper, thermodynamic equilibria

Received: December 2, 2022

Revised: February 3, 2023

Published online: March 2, 2023

- [1] J. W. Choi, B. Shin, P. Gorai, R. L. Z. Hoyer, R. Palgrave, *ACS Energy Lett.* **2022**, 7, 1553.
- [2] B. Saparov, *Chem. Rev.* **2022**, 122, 10575.
- [3] S. J. Adjogri, E. L. Meyer, *Materials* **2021**, 14, 7857.
- [4] K. V. Sopiha, C. Comparotto, J. A. Márquez, J. J. S. Scragg, *Adv. Opt. Mater.* **2022**, 10, 2101704.
- [5] S. Perera, H. Hui, C. Zhao, H. Xue, F. Sun, C. Deng, N. Gross, C. Milleville, X. Xu, D. F. Watson, B. Weinstein, Y. Y. Sun, S. Zhang, H. Zeng, *Nano Energy* **2016**, 22, 129.
- [6] S. Niu, B. Zhao, K. Ye, E. Bianco, J. Zhou, M. E. McConney, C. Settens, R. Haiges, R. Jaramillo, J. Ravichandran, *J. Mater. Res.* **2019**, 34, 3819.
- [7] A. Swarnkar, W. J. Mir, R. Chakraborty, M. Jagadeeswararao, T. Sheikh, A. Nag, *Chem. Mater.* **2019**, 31, 565.
- [8] Y. Y. Sun, M. L. Agiorgousis, P. Zhang, S. Zhang, *Nano Lett.* **2015**, 15, 581.
- [9] D. Tiwari, O. S. Hutter, G. Longo, *J. Phys.: Energy* **2021**, 3, 034010.
- [10] J. Xu, Y. Fan, W. Tian, L. Ye, Y. Zhang, Y. Tian, Y. Han, Z. Shi, *J. Solid State Chem.* **2022**, 307, 122872.
- [11] Z. Huo, S. H. Wei, W. J. Yin, *J. Phys. D: Appl. Phys.* **2018**, 51, 474003.
- [12] E. Osei-Agyemang, G. Balasubramanian, *ACS Appl. Energy Mater.* **2020**, 3, 1139.
- [13] S. Niu, J. Milam-Guerrero, Y. Zhou, K. Ye, B. Zhao, B. C. Melot, J. Ravichandran, *J. Mater. Res.* **2018**, 33, 4135.
- [14] C. Comparotto, P. Ström, O. Donzel-Gargand, T. Kubart, J. J. S. Scragg, *ACS Appl. Energy Mater.* **2022**, 5, 6335.
- [15] Y. Wang, N. Sato, T. Fujino, *J. Alloys Compd.* **2001**, 327, 104.
- [16] M. Saeki, Y. Yajima, M. Onoda, *J. Solid State Chem.* **1991**, 92, 286.
- [17] Y. C. Hung, J. C. Fetting, B. W. Eichhorn, *Acta Crystallogr., Sect. C: Cryst. Struct. Commun.* **1997**, 53, 827.
- [18] B.-H. Chen, W. Wong-Ng, B. W. Eichhorn, *J. Solid State Chem.* **1993**, 103, 75.
- [19] B. Chen, B. W. Eichhorn, P. E. Fanwick, *Inorg. Chem.* **1992**, 31, 1788.
- [20] W. Li, S. Niu, B. Zhao, R. Haiges, J. Ravichandran, A. Janotti, *Phys. Rev. Mater.* **2019**, 3, 101601.
- [21] Y. Li, D. J. Singh, *Eur. Phys. J. B* **2018**, 91, 188.
- [22] C. Ming, K. Yang, H. Zeng, S. Zhang, Y.-Y. Sun, *Mater. Horiz.* **2020**, 7, 2985.
- [23] A. Jain, S. P. Ong, G. Hautier, W. Chen, W. D. Richards, S. Dacek, S. Cholia, D. Gunter, D. Skinner, G. Ceder, K. A. Persson, *APL Mater.* **2013**, 1, 011002.
- [24] A. J. Jackson, A. Walsh, *J. Mater. Chem. A* **2014**, 2, 7829.
- [25] A. J. Jackson, A. Walsh, *Phys. Rev. B* **2013**, 88, 165201.
- [26] Y. Nishigaki, T. Nagai, M. Nishiwaki, T. Aizawa, M. Kozawa, K. Hanzawa, Y. Kato, H. Sai, H. Hiramatsu, H. Hosono, H. Fujiwara, *Sol. RRL* **2020**, 4, 2070051.
- [27] I. Pallikara, P. Kayastha, J. M. Skeleton, L. D. Whalley, *Electron. Struct.* **2022**, 4, 033002.
- [28] X. Wu, C. Ming, J. Shi, H. Wang, D. West, S. Zhang, Y.-Y. Sun, *Chin. Phys. Lett.* **2022**, 39, 046101.
- [29] T. Nitta, K. Nagase, S. Hayakawa, *J. Am. Ceram. Soc.* **1970**, 53, 601.
- [30] M. Ishii, M. Saeki, M. Sekita, *Mater. Res. Bull.* **1993**, 28, 493.
- [31] N. Gross, Y.-Y. Sun, S. Perera, H. Hui, X. Wei, S. Zhang, H. Zeng, B. A. Weinstein, *Phys. Rev. Appl.* **2017**, 8, 044014.
- [32] K. Ye, N. Z. Koocher, S. Filippone, S. Niu, B. Zhao, M. Yeung, S. Bone, A. J. Robinson, P. Vora, A. Schleife, L. Ju, A. Boubnov, J. M. Rondinelli, J. Ravichandran, R. Jaramillo, *Phys. Rev. B* **2022**, 105, 195203.
- [33] C. Toulouse, D. Amoroso, C. Xin, P. Veber, M. C. Hatnean, G. Balakrishnan, M. Maglione, P. Ghosez, J. Kreisel, M. Guennou, *Phys. Rev. B* **2019**, 100, 134102.
- [34] M. Ishigame, T. Sakurai, *J. Am. Ceram. Soc.* **1977**, 60, 367.
- [35] V. G. Keramidias, W. B. White, *J. Am. Ceram. Soc.* **1974**, 57, 22.
- [36] K. H. Rieder, B. A. Weinstein, M. Cardona, H. Bilz, *Phys. Rev. B* **1973**, 8, 4780.
- [37] D. De Waal, K. J. Range, M. Königstein, W. Kiefer, *J. Raman Spectrosc.* **1998**, 29, 109.
- [38] A. Jain, S. P. Ong, G. Hautier, W. Chen, W. D. Richards, S. Dacek, S. Cholia, D. Gunter, D. Skinner, G. Ceder, K. A. Persson, *APL Mater.* **2013**, 1, 11002.
- [39] W. Sun, S. T. Dacek, S. P. Ong, G. Hautier, A. Jain, W. D. Richards, A. C. Gamst, K. A. Persson, G. Ceder, *Sci. Adv.* **2016**, 2, 1600225.
- [40] M. Aykol, S. S. Dwaraknath, W. Sun, K. A. Persson, *Sci. Adv.* **2018**, 4, <https://doi.org/10.1016/j.scriptamat.2015.07.021>.
- [41] V. Blum, R. Gehrke, F. Hanke, P. Havu, V. Havu, X. Ren, K. Reuter, M. Scheffler, *Comput. Phys. Commun.* **2009**, 180, 2175.
- [42] M. O. Lenz, T. A. R. Purcell, D. Hicks, S. Curtarolo, M. Scheffler, C. Carbogno, *NPJ Comput. Mater.* **2019**, 5, 123.
- [43] J. P. Perdew, A. Ruzsinszky, G. I. Csonka, O. A. Vydrov, G. E. Scuseria, L. A. Constantin, X. Zhou, K. Burke, *Phys. Rev. Lett.* **2008**, 100, 136406.
- [44] A. V. Krukau, O. A. Vydrov, A. F. Izmaylov, G. E. Scuseria, *J. Chem. Phys.* **2006**, 125, 224106.
- [45] A. Togo, I. Tanaka, *Scr. Mater.* **2015**, 108, 1.
- [46] J. M. Skelton, L. A. Burton, A. J. Jackson, F. Oba, S. C. Parker, A. Walsh, *Phys. Chem. Chem. Phys.* **2017**, 19, 12452.
- [47] H. Shang, N. Raimbault, P. Rinke, M. Scheffler, M. Rossi, C. Carbogno, *New J. Phys.* **2018**, 20, 73040.
- [48] J. P. Perdew, K. Burke, M. Ernzerhof, *Phys. Rev. Lett.* **1996**, 77, 3865.
- [49] P. Kayastha, A. Jackson, L. D. Whalley, *ThermoPot*, Zenodo **2022**, <https://doi.org/10.5281/zenodo.7351356>.